Advanced Computational Modeling of Vapor Deposition in a High-Pressure Reactor

Beatriz H. Cardelino
Spelman College
cardelino@spelman.edu

Craig E. Moore
NASA Marshall Space Flight Center
craig.e.moore@nasa.gov

Sonya D. McCall
Spelman College
smccall@spelman.edu

Carlos A. Cardelino
Georgia Inst. of Technology
carlos@eas.gatech.edu

Nikolaus Dietz
Georgia State University
ndietz@gsu.edu

Klaus Bachmann
North Carolina State University
k_bachmand@ncsu.edu

Abstract

In search of novel approaches to produce new materials for electro-optic technologies, advances have been achieved in the development of computer models for vapor deposition reactors in space. Numerical simulations are invaluable tools for costly and difficult processes, such as those experiments designed for high pressures and microgravity conditions. Indium nitride is a candidate compound for high-speed laser and photo diodes for optical communication system, as well as for semiconductor lasers operating into the blue and ultraviolet regions. But InN and other nitride compounds exhibit large thermal decomposition at its optimum growth temperature. In addition, epitaxy at lower temperatures and subatmospheric pressures incorporates indium droplets into the InN films. However, surface stabilization data indicate that InN could be grown at 900 K in high nitrogen pressures, and microgravity could provide laminar flow conditions. Numerical models for chemical vapor deposition have been developed, coupling complex chemical kinetics with fluid dynamic properties.

1. Introduction.

The possibility of developing blue or ultraviolet (UV) light emitting diodes (LEDs) and laser diodes, as well as high-frequency transistors operating at high powers and temperature, has generated much interest in group IIIA-nitride compounds (e.g., InN, GaN, and AlN) [1]. These materials are mainly produced by metallo-organic vapor phase epitaxy (MOVPE) and molecular beam epitaxy (MBE) [2]. The most studied group IIIA-nitride compound is GaN [3], but in recent years, the number of publications concerning InN has increased significantly due to its unique properties [4]. For example, incorporation of small concentrations of In in GaN considerably increases luminescence efficiency [5] and $In_xGa_{1-x}N$ quantum wells are the core of high-efficiency LEDs operating in the green to violet region. Monte Carlo calculations [6] have predicted: (a) that InN exhibits extremely high peak drift velocity at room temperature and a saturation velocity much larger than GaN, resulting in much better transport characteristics over a wide range of temperature and doping concentrations; (b) that InN exhibits the highest peak overshoot velocity lasting over the longest distance when compared with GaN and AlN; (c) that InN has an extremely high speed with a cutoff frequency of over 1 THz for 0.1 μm gates in field-effect transisors (FETs). Thus, its transport properties suggest that there may be advantages for using InN in high frequency centimeter and millimeter wave devices over GaN; its transient electron transport properties suggest that it may be better than GaN in submicron-scale devices, where transient transport is the dominant mechanism; and, that InN is a highly potential material for the fabrication of high-speed high-performance heterojunction FETs.

Until recently, the accepted optical band gap energy for InN was 1.89 eV at room temperature [7]. But, single crystalline high quality hexagonal InN films grown by MBE showed a band gap energy between 0.65 and 0.90 eV, measured by optical absorption, photoluminescence, photoluminescence excitation and photoreflectivity [8-9]. Assuming that the larger band gap is correct, then the emission at around 0.7 eV may be interpreted as deep level emissions [10]. Conversely, assuming that the narrower band gap is correct, then the emission at 1.9 eV may be attributed to the presence of oxynitrides [11]. The lower band gap value of 0.7 eV is

compatible with the wavelength of optical fibers. diodes for optical communication system is another possible application for InN. To make such devices, p-type InN would be essential. But the undoped InN film usually displays high n-type conductivity. Mg doping has been attempted unsuccessfully in search of p-type InN [12-13]. Also, the highest mobility and lowest background carrier concentrations achieved in MOVPE [14] are 730 cm^2 V^{-1} s^{-1} and $5.8x10^{18}$ cm^{-3}, respectively, and in MBE [15] are 2050 cm^2 V^{-1} s^{-1} and $3.49x10^{17}$ cm^{-3}, respectively. For comparison, the highest mobility and lowest background carrier concentrations reported for GaN are 950 cm^2 V^{-1} s^{-1} and $8x10^{16}$ cm^{-3}, respectively [16]. Recently, strong photoluminescence has been observed in InN films grown on silicon substrates [17].

InN is the most difficult group IIIA-nitride to grow because the equilibrium vapor pressure of nitrogen over InN is much higher than over AlN and GaN. Figure 1 shows the equilibrium N_2 pressures versus inverse temperature, using linear fit equations obtained by Ambacher et al. [18] from high pressure data and theoretical calculations.

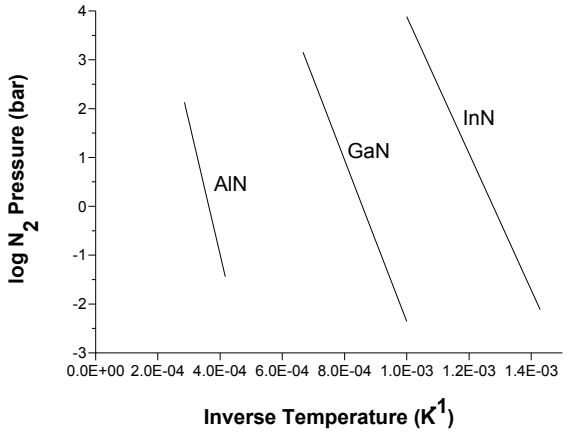

Figure 1. Equilibrium N_2 pressures over the group IIIA-N solid, from high pressure experiments and theoretical calculations.

Epitaxial growth of single crystalline and good quality InN films was widely studied in the 1990s. These studies included MOVPE and MBE on different substates and underlying layers, over a wide range of growth conditions. Because of the low InN dissociation temperature and high equilibrium N_2 vapor pressure over the InN film, the preparation of InN requires growth temperatures lower than 770 K. However, growth below 670 K and subatomic pressures is dominated by the formation of metallic In droplets. The growth temperature is the most critical parameter to control film quality. It influences Thus, fabrication of high-speed laser and photo crystallinity, surface morphology, growth rate, and electrical properties. But growth pressure is also a basic parameter, especially affecting the electrical properties of the InN film. In conventional MOVPE, the temperature range is usually 820-920 K, with either atmospheric or subatmospheric (76 torr) presure.

The source materials generally used for MOVPE growth of InN are trimethylindium (TMI) and ammonia (NH_3), with N_2 as the carrier gas. If the temperature of the substrate needs to be reduced to prevent InN decomposition, a way of increasing TMI dissociation is to reduce the flow rate. But, to maintain laminar flow, a condition that is required for homogeneous epitaxy, the Grashof number (G_r) must be much smaller than the square of the Reynolds number (R_e), as defined by equations 1 and 2:

$$G_r = \frac{h^3 \mathbf{g} \rho^2 \beta_T \Delta T}{\mu^2} \qquad [1]$$

$$R_e = \frac{\rho \mathbf{u} h}{A \mathbf{P} \mu} \qquad [2]$$

where h is the channel height, **g** the gravity vector, ρ the density of the fluid, β_T the volume coefficient of expansion, ΔT the change in temperature in the channel, μ the viscosity of the gas, **u** the standard flow rate, A the cross-sectional area, and **P** the standard pressure. From equations 1 and 2 it can be seen that the G_e/R_e^2 ratio is proportional to **g** $(\mathbf{P}/\mathbf{u})^2$. Therefore, on the ground, high pressure MOVPE must be carried out at a sufficiently high flow velocity to maintain a small G_e/R_e^2 ratio. Alternatively, under conditions of reduced gravity, an increase in **P** could be coupled with a smaller **u** without an onset of turbulence. Furthermore, higher N_2 pressures can suppress nitrogen evaporation from the grown InN film, according the the following equation:

$$InN\ (s) \rightarrow In\ (\ell) + \tfrac{1}{2}\ N_2\ (g) \qquad [3]$$

In the context of a need for extending MOVPE processing to elevated pressures, new reactor designs have been built that cover the pressure range 10^{-2} to 10^2 atm. These reactors are now available for both scientific studies and process development at Georgia State University. Although MOVPE processes at elevated pressure can be studied on the ground, there are significant limits in the choice of conditions related to onset of turbulence. This is particularly important in a reactor with forced channel flow operating at elevated pressure, in the range of Reynolds numbers greater than one thousand. Turbulence is known to introduce fluctuations in vapor

density on a wide range of spatial and time scales. The reduction of the Grashof number in a microgravity environment by several orders of magnitude relaxes the requirement of fast linear flow velocity in the channel, and thus allows experimentation at Reynolds numbers well below the critical value of one thousand, that is, under conditions of well-behaved flow.

Experiments to be performed in space are difficult to perform, costly, and cannot be performed repeatedly. Simulations of fluid dynamics coupled to chemical reactions, transport, adsorption and surface reactions that result in epitaxial crystal growth have been helpful in both reactor and process design. Stringfellow and co-workers first proposed a model to predict the composition of IIIA-VA alloys by MOVPE, assuming thermodynamic equilibrium [19]. A thermodynamic approach was used by Koukitu and Seki [20] to study IIIA-VA semiconductor alloys, and their model included a constraint regarding equilibrium partial pressures for the major species. On the other hand, Mountziaris and Jensen developed a kinetic model for GaAs from trimethylgallium and arsine [21]. The general thermodynamic model was recently applied by Asai and Dandy [22] to a systematic study of IIIA-VA semiconductor alloy deposition, including nitrides grown by MOVPE. A model based on 2D steady-state Navier-Stokes equations of fluid dynamics and gas-phase chemical reactions has been used to simulate MOVPE deposition of InGaN, by Talalaev et al. [23]. Similarly, Carr et al. have used the Chemkin [24] program to study the trimethylgallium and ammonia chemical vapor deposition process [25].

However, the set of input parameters for such computations still requires refinements, which motivated the research discussed here. We expect that in a microgravity environment validations of the models and input parameters will be possible, without the ambiguities inherent to simulations of turbulent flow. The ultimate goal of the numerical simulations presented here is to address the following specific questions:

1. To what maximum temperature can the decomposition of InN be extended by processing in a microgravity environment at a pressure of 100 atm?
2. How does the shift of the decomposition of source vapor molecules from the surface of the heated substrate into the adjacent gas phase affect the kinetics of heteroepitaxial growth in microgravity at high pressure?
3. How does the kinetics of heteroepitaxial overgrowth respond to changes from laminar to turbulent flow?
4. What differences exist in steady-state heteroepitaxial growth for laminar and turbulent flow?
5. Is it possible to devise reduced order models that permit the simulation of processes that are executed under conditions of turbulent flow on the ground?

2. Methods.

In MOVPE, a reactive gas flow that is transported through a reactor chamber, undergoes gas-phase reactions and/or surface reactions at a substrate. In both cases, the precursors become adsorbed at the surface, diffuse, and nucleate resulting in film growth. Even after a decade of experience in MBE and MOCVE growth, there is uncertainty regarding many of the processes that take place during film growth since the diagnostic tools used in surface science usually cannot be applied under the conditions of the reaction chamber. In order to bring advancement in the field of crystal growth processes, there is increasing interest in pursuing integrated approaches towards intelligent modeling, design and control of crystal growth processes. The thrust of these efforts is to develop models that can account for all important phenomena associated with the growth process, which may be used as a predictive design tool to achieve optimal process conditions including those processing conditions that are outside the reach of conventional chemical vapor deposition.

These processes are usually classified as occurring at three length and time scales. At the macroscopic level, the simulations address growth rate, film composition and film uniformity. At the mesoscopic level, the simulations involve prediction of detailed surface morphology. At the microscopic level, the simulations account for adsorption, diffusion and chemical reactions at the substrate. All three levels are required to predict the characteristics of the epitaxy. The present investigation involves macroscopic simulations that utilize parameters obtained from microscopic models.

The macroscopic simulations solve the conservation equations describing fluid flow, heat and mass transfer, coupled with homogeneous and heterogeneous chemical reactions that are modeled under steady-state conditions. The simulations require previous knowledge of various parameters as a function of temperature and pressure: transport properties of the species (e.g., thermal conductivity, diffusion and viscosity coefficients), thermochemical properties of the species (e.g., molecular heat capacity, enthalpy and entropy), as well as homogeneous and heterogeneous reaction rate constants. These continuum models are performed in two or three-dimensions, using a finite difference approach. At the

microscopic level, molecular orbital calculations are used, based on density functional theory, to obtain information regarding the structure of single molecules, as well as their electronic, vibrational and rotational energies. These properties, combined with statistical thermodynamics, are used to determine the thermochemical properties of the species. Molecular mechanic calculations, performed on multiple molecules, are used to determine the transport properties of the species. In addition, quantum chemistry calculations, together with transition state theory, are used to predict reaction rate constants.

Numerical simulations have been performed using an existing general-purpose commercial software, CFD-ACE [26]; developed by CFD Research Corporation of Huntsville, Alabama. The governing equations that are solved by CFD-ACE consist of conservation laws for mass, momentum, energy, and species, as well as models for thermodynamic and transport properties, and chemical reactions. The physical and chemical models in CFD-ACE that are relevant to the modeling of vapor deposition are: (a) a multi-component transport model [27], (b) a thermal radiation model computed based on the solution of the Navier-Stokes equations [28], (c) a gas phase chemistry model using rate coefficients that have an Arrhenius form of the type

$$k = A\ T^{n} \exp\left(-\frac{E_a}{kT}\right) \qquad [4]$$

being n and E_a constants for each reaction, and A (the pre-exponential factor) that may have a pressure and temperature dependence, and (d) a surface chemistry model to account for chemistry between surface adsorbed species.

The numerical simulations involve chemical kinetics and fluid dynamics considerations. The two aspects of the numerical simulations are summarized in Figure 2. From the chemical kinetics point of view, (a) the elementary steps that constitute the chemical mechanism must be selected; (b) the temperature and pressure-dependent thermodynamic properties must be obtained for all gas species included in the elementary steps; (c) the temperature and pressure-dependent reaction rate constants must be obtained for all gaseous and heterogeneous reactions; and (d) the physical parameters necessary for the fluid dynamics simulations (viscosity, thermal conductivity, and diffusivity) must be obtained.

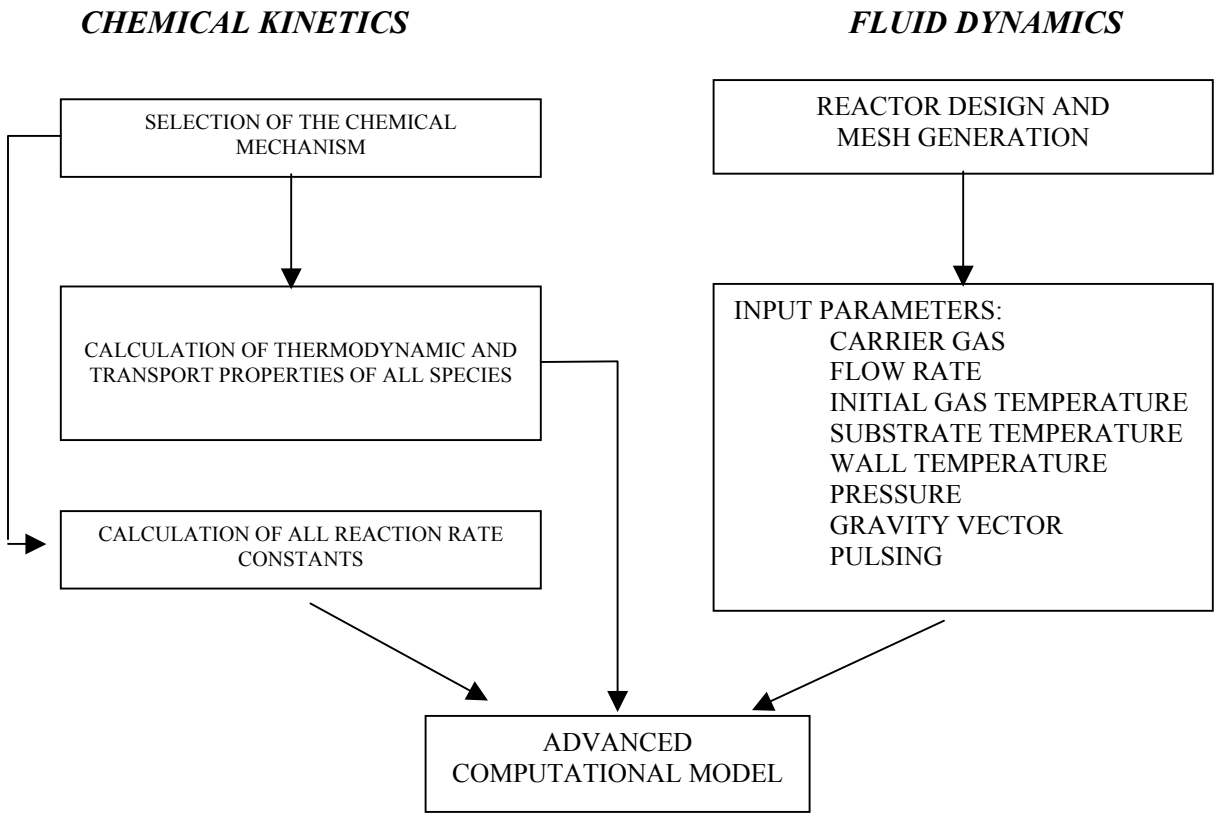

Figure 2. Scheme for performing an advanced computational model

In previous work we have shown that density functional theory can adequately predict electronic energies for indium compounds within a few kiloJoules per mole and harmonic frequencies within 10% of experimental values [29]. Using the results of those calculations, and by applying statistical thermodynamics, we have estimated the thermodynamic properties of many indium compounds, for which we published the corresponding JANAF parameters [30] at atmospheric pressure. In those calculations, we have included secondary effects (such as internal rotations, excited electronic states and anharmonicity corrections, as well as real gas corrections) that may be of consequence at conditions of high temperature and pressure. All electronic and vibrational calculations were performed with the quantum mechanical program Gaussian 2003 [31].

Previously, we have developed a procedure for calculating reaction rate constants for the homolytic dissociation of group IIIA and group VA compounds based on quantum mechanical calculations and transition state theory [32]. The procedure uses a novel semiclassical approach for determining the critical configuration, whereas quantum mechanics is used to determine the characteristics of the initial and final states. Comparison of predicted reaction rate constants with eleven experimentally determined values showed that our predictions were within 100 times the experimental values. The comparison included free radical dissociations and some high-pressure dissociation reactions. The accuracy of the predictions compares very well with the uncertainty of the experimental data.

With respect to the fluid dynamic aspects, a reactor design and input conditions must be selected. In this investigation, the design was based on the compact hard-shell reactor for high pressures of Georgia State University. This reactor was built to withstand pressures up to 100 atm. Two identical inner core halves are placed on top of each other and inserted into the pressure bearing reactor shell. The reactor thus features machined inner walls, grading in and out of the entrance and exit ports, such that the flow channel formed has constant cross section from entrance to exit. Two substrate prisms heated from the back are made part of the top and bottom channel walls. Therefore, the divergence of nutrient fluxes to these substrate crystals in the top and bottom channel walls is symmetric to the centerline. The reactor is 12 inches long and has, at the substrate location, an inner channel height and width of 1 mm and 50 mm, respectively.

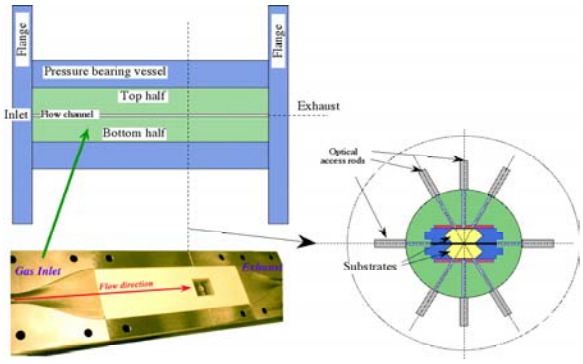

Figure 3. Schematic representation of the axial cross section (xz plane) of the compact hard-shell reactor for pressure up to 100 atm from Georgia State University.

In CFD-ACE, the magnitude and direction of the gravity vector is an input parameter. It should be noted that at high pressures, homogeneous bimolecular reaction kinetics, resulting in adducts of fragments that are important intermediaries in low pressure MOVPE, may be irrelevant. Furthermore, pulsed injection of the group IIIA and group VA source vapors, separated by plugs of pure carrier gas, may prevent homogeneous nucleation of IIIA-VA compound particles in the vapor phase. But, the separate arrival of group IIIA and group VA precursors on the surface of the heated substrates of the reactor may require conditions of forced flow in a channel reactor so that re-circulation is prevented.

3. Results.

Results on the gas-phase dissociation of trimethylindium (TMI) are reported based on the following models: a) a strictly thermodynamic model; b) a strictly chemical kinetic model; c) an advanced chemical kinetic/fluid dynamic numerical simulation in an MOVPE reactor. Finally, advances on the InN deposition in a MOVPE reactor are also reported.

3.1 Thermodynamic model of TMI dissociation

Reactions [5] through [11] were considered for the thermodynamic model, including TMI, dimethylindium (DMI), singlet and triplet monomethylindium (MMI), atomic indium (In), methyl radical (CH_3) and ethane (C_2H_6). The dissociation constants were calculated as discussed

under Methods, at four conditions of temperature and pressure: 1 atm and 20 atm, and at 300 and 1000 K. These conditions were selected to compare the results under normal conditions of pressure and temperature with conditions of high pressure and/or temperature.

$TMI \rightarrow DMI + CH_3$	K_1	[5]
$DMI \rightarrow MMI\ singlet + CH_3$	K_2	[6]
$DMI \rightarrow MMI\ triplet + CH_3$	K_3	[7]
$MMI\ singlet \rightarrow In + CH_3$	K_4	[8]
$MMI\ triplet \rightarrow In + CH3$	K_5	[9]
$MMI\ singlet \rightarrow MMI\ triplet$	K_6	[10]
$CH_3 + CH_3 \rightarrow C_2H_6$	K_7	[11]

The thermodynamic model resulted in complete dissociation for TMI at 300K. See Figure 4. Under the four conditions studied, TMI mostly dissociates into singlet monomethylindium (MMI). Higher pressure increased the mole fraction of atomic In. Triplet MMI is not shown in Figure 4 because its mole fraction was negligible compared to singlet MMI.

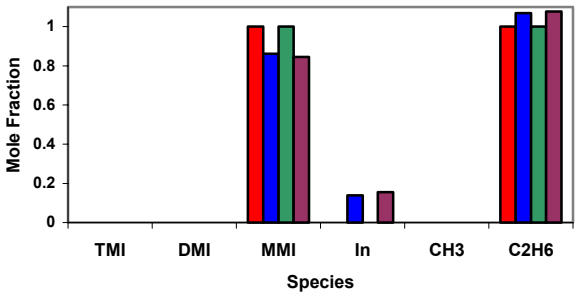

Figure 4. Dissociation of trimethylindium (TMI) based on a strictly thermodynamic model, at four conditions of pressure and temperature.
DMI=dimethylindium, MMI=singlet monomethyl-indium.
Red: pressure = 1 atm, temperature = 300 K; blue: pressure = 20 atm, temperature = 300 K; green: pressure = 1 atm, temperature = 1000 K; violet: pressure = 20 atm, temperature =1000 K.

A similar analysis on trimethylaluminum (TMA) and trimethylgallium (TMG) at 300 K resulted in a fully undissociated TMA and only 0.4% dissociation of TMG into monomethylgallium (MMG). At 1000 K, there was 0.1% TMA dissociation into monomethylaluminum (MMA) and 17% dissociation of TMG into MMG. There is experimental evidence that TMI, TMG and TMA do not dissociate at 300K. Thus, these results seem to indicate that TMA and TMG do not dissociate at 300 K because of thermodynamic reasons, whereas TMI does not dissociate because of the kinetics of its dissociation. To confirm this hypothesis, a strictly chemical kinetic model was solved by finite differences.

3.2 Chemical kinetic model of TMI dissociation

A strictly chemical kinetic system of equations was solved for the dissociation of TMI, using reactions [5], [6], [8] and [11]. The reaction rate constants were calculated as described under Methods. The dissociation of TMI at 300 K was calculated up to $1.4x10^5$ s, using increasing time increments from $2x10^{-11}$s to 1000 s. No dissociation of TMI was detected.

Figure 5 shows the results obtained after 2 nanoseconds, using a time increment of $2x10^{-11}$ s, for temperatures ranging from 500 to 900 K. Initially, TMI dissociation favors DMI over MMI and atomic In. But an increase in temperature affects more the concentration of atomic In than the concentrations of MMI or DMI: about 50, 29 and 25 mmoles per K, respectively. Also, the increase in pressure from 1 atm to 20 atm increases the initial mole fraction of atomic In, MMI and DMI by factors of 10,000, 1,000, and 100, respectively.

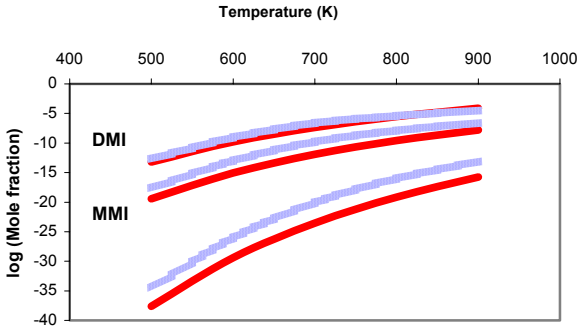

Figure 5. Dissociation of trimethylindium (TMI) after 2 nanoseconds, based on a strictly chemical kinetic model, at 1 atm and 20 atm, as a function of temperature,. Dark lines: pressure = 1 atm; gray lines: pressure = 20 atm.

Figure 6 shows the results obtained with the strictly chemical kinetic model based on reactions [5], [6], [8] and [11], after 0.1 s, using a time increment of $1x10^{-4}$ s, at four conditions of temperature and pressure: 1 atm and 20 atm, and at 850 and 1000 K. At 850 K, both pressures showed

about 4% TMI dissociation, and ratios of MMI to atomic In to DMI of about 120:12:1. At 1000 K, both pressures showed about 72% TMI dissociation, and ratios of MMI to atomic In to DMI of about 180:100:1. Since TMI did not dissociate at 300 K, case is not shown in Figure 6.

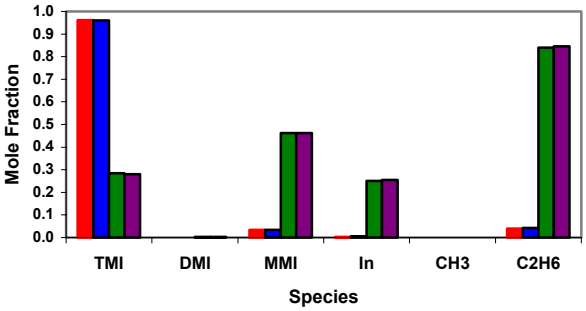

Figure 6. Dissociation of trimethylindium (TMI) based on a strictly chemical kinetic analysis, after 0.1 seconds. Solid black: pressure = 1 atm, temperature = 850 K; dark gray: pressure = 20 atm, temperature = 850 K; light gray: pressure = 1 atm, temperature = 1000 K; striped: pressure = 20 atm, temperature = 1000 K.

In summary, the strictly kinetic models showed: a) a dramatic change in TMI dissociation between 850 and 1000 K; b) negligible DMI concentrations; and, c) an increase in atomic In with increasing temperature or pressure.

3.3 Chemical kinetic / fluid dynamic model of TMI dissociation

Numerical simulations of the dissociation of TMI in a MOVPE reactor were performed using the general purpose computational-fluid-dynamics code CFD-ACE. The physical characteristics of the model were based on an existent compact hard-shell reactor. As discussed under Methods, CFD-ACE can simulate multi-species transport, heat and mass transfer (including thermal radiation), fully coupled gas phase and surface chemistry for conventional chemical vapor deposition reactors. The simple system of reactions chosen to simulate the dissociation of trimethylindium were reactions [5] through [11]. No species with two In atoms were included (i.e., no In-In bond formation). No C-H bond breaking was assumed to occur, since that bond breaking requires more energy than an In-C dissociation (about 300 and 200 kJ mol^{-1}, respectively). The only species with more than one multiplicity considered was MMI, which may be a singlet or a triplet with a difference in energy of 190 kJ mol^{-1}.

The modeling required three types of parameters: (a) reaction rate constants; (b) thermodynamic properties for all species, and (c) transport properties for all species. The first two types of parameters were obtained as discussed under Methods. The transport properties were estimated from parameters of the 6-12 Lennard-Jones and Sutherland potentials. The Sutherland parameters were obtained from the values of the 6-12 Lennard-Jones potential at intermolecular distances greater than 10Å. The simulations only involve homogeneous gas phase reactions, based on the assumption that the substrate surface provided no sinks for the dissociation products of the organometallic compound formed in the vapor phase, that is, that no deposition occurred at the substrate.

The boundary conditions on the momentum equations specified no slip at the solid walls. Simple thermal boundary conditions were based on the assumption of adiabatic outer wall temperatures. All walls were set to 300 K, whereas the substrate walls were set to 1000 K. The operating conditions corresponded to a flow dominated by forced convection (where the Grashof number was much smaller than the square of Reynolds number). We assumed a parabolic inlet flow velocity of 12 standard liters per minute (slm) and a constant inlet gas temperature of 300 K. The carrier gas was N_2, with a flow rate of 12 standard liters per minute, and a mass fraction for TMI of $2x10^{-4}$. The reactor consisted of a grid of 90,657 cells and 109,570 nodes, with the concentration of grid cells larger in the region of the substrate.

The gas phase reactions of TMI were obtained in the pressure range of 1 to 20 atm, under steady-state conditions. At the leading edge of the substrate, and at 1 atm, TMI is the main species present. At 2.5 atm, there is as much TMI as MMI, and at higher pressures MMI is about 90%. Thus, increasing pressure promotes MMI formation at the leading edge of the substrate.

The predicted mole fractions at the center of the substrate, as a function of pressure, are shown in Figure 7. At 1 atm, there is 40% TMI and 58% MMI. A maximum of 93% MMI occurs at 2.5 atm. Increasing pressures reduce MMI mole fraction, while increasing atomic In. For pressures above 12.5 atm, the mole fraction for atomic In predominates, and at 20 atm there is 70% atomic In and 30% MMI.

The trailing edge of the substrate shows 30% TMI, 70% MMI at 1 atm, then few percent higher atomic In fractions than the center of the substrate for pressures below 12.5 atm, and finally few percent higher MMI fractions than the center of the substrate for pressures above 12.5 atm.

We interpret the results as follows: the increase in temperature favors dissociation of TMI into MMI and the increase in pressure favors dissociation of MMI into atomic In. These results regarding the dissociation of TMI clearly demonstrated the need of an advanced chemical/fluid dynamic model to simulate the MOVPE of InN. A comparison between the results from the simulation of the dissociation of TMI and experimental measurements taken between the range of 1 to 20 atm is under way.

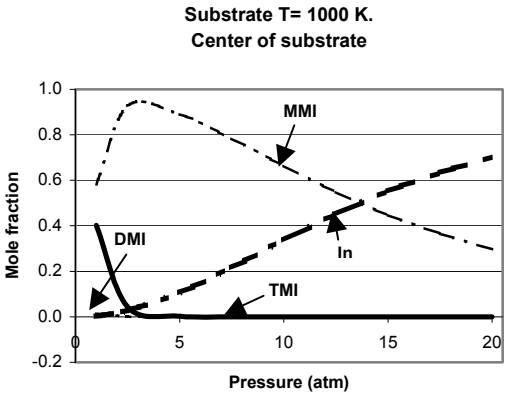

Figure 7. Dissociation of TMI in a MOVPE reactor, based on a chemical kinetic/fluid dynamic model, under steady-state conditions, as a function of pressure.

3.3 Advances on a chemical kinetic / fluid dynamic model of InN deposition

An advanced computational model was developed to predict the formation InN film from the reaction of TMI with ammonia (NH_3)[33]. Both components were introduced into the reactor in the gas phase. The background gas was molecular nitrogen (N_2). Organometallic chemical vapor deposition occured on a heated sapphire surface. The InN film was collected onto a hot sapphire substrate. The overall reaction between the two reactants can be sketched as:

$$TMI_{gas} + NH_{3\ gas} \rightarrow\rightarrow InN_{film} + 3\ CH_{3\ gas} + 3\ H_{gas} \qquad [12]$$

The methyl and hydrogen radicals could combine to form methane (CH_4), ethane (C_2H_6) or molecular hydrogen (H_2). The InN film could decompose as shown by reaction [3].

There are many possible reacting species for the system described. As a first approximation, only two indium reactive species were selected: MMI for the formation of InN, and TMI for the formation of the TMI:NH_3 adduct. Similarly, only two nitrogen reactive species were chosen: triplet NH for the formation of InN, and NH_3 for the formation of the adduct. NH was generated by a two-step photolysis of NH_3 in the vicinity of the substrate, which is technically attainable. The formation of the TMI:NH_3 adduct was assumed to occur in the gas phase while the thermal decomposition of TMI either occurred in the gas phase or on a TMI molecule adsorbed to the surface. In the simulations, InN could be formed either in the gas phase and subsequently adsorbed to the surface, or by direct reaction of an adsorbed MMI with gaseous NH. In either case, InN could undergo decomposition, a process that was strongly dependent on pressure. The thermodynamic and transport properties of the species, as well as the reaction rate constants, were determined as discussed under Methods.

Three basic chemical mechanisms for InN film formation were considered. In all three mechanisms, TMI thermally dissociated in the gas phase to MMI (reaction [13]), NH_3 spectroscopically dissociated to NH (reaction [14]), and MMI reacted with NH homogeneously to form InN gas (reaction [15]). InN gas deposited onto the sapphire surface to form InN film (reaction [16]). In addition to reactions [13] to [16], Mechanism II included adsorption of MMI to the surface (reaction [17]) which further reacted with NH to form InN film (reaction [18]). In addition to reactions [13] to [18], Mechanism III included the adsorption of TMI to the sapphire surface (reaction [19]), followed by dissociation into adsorbed MMI (reaction [20]), and reaction of the bound MMI with the NH radical to form InN film (reaction [21]). In all three mechanisms, the CH_3 and H radicals combine to form CH_4 (reaction [22]). The main competing reaction to the MMI and NH reaction was the formation of the TMI:NH_3 adduct (reaction [23]). Formation of this adduct was included as part of the three mechanisms. The incoming reactants (TMI and NH_3) were introduced into the reactor under two regimes: simultaneously and in pulses. The pulsing case was designed to minimize adduct formation. It is important to note that the three mechanisms did not

consider InN film dissociation. Future computations will include InN dissociation and its N_2 pressure dependence (see equation [3]). Only runs with N_2 at 1 atm were considered.

$TMI_{gas} \Leftrightarrow DMI_{gas} + CH_{3\,gas} \Leftrightarrow$
$MMI_{gas} + 2\,CH_{3\,gas}$ [13]

$NH_{3\,gas} \rightarrow NH_{2\,gas} + H_{gas} \rightarrow$
$NH\,gas + 2\,H_{gas}$ [14]

$MMI_{gas} + NH_{gas} \rightarrow InN_{gas} + CH_{4\,gas}$ [15]

$InN_{gas} \rightarrow InN_{film}$ [16]

$MMI\ gas \rightarrow MMI\ adsorbed$ [17]

$MMI_{adsorbed} + NH_{gas} \rightarrow InN_{film} + CH_{4\,gas}$ [18]

$TMI_{gas} \rightarrow TMI_{adsorbed}$ [19]

$TMI_{adsorbed} \Leftrightarrow DMI_{adsorbed} + CH_{3\,gas}$
$\Leftrightarrow MMI_{adsorbed} + 2\,CH_{3\,gas}$ [20]

$MMI_{adsorbed} + NH_{gas} \rightarrow$
$InN_{film} + CH_{4\,gas}$ [21]

$CH3_{gas} + H_{gas} \rightarrow CH_{4\,gas}$ [22]

$TMI_{gas} + NH_{3\,gas} \Leftrightarrow TMI{:}NH_{3\,gas}$ [23]

The model reactor (see Figure 3) consisted of a chamber 36 cm long. The inlet and outlet had square cross section of 1.5 cm by 1.5 cm, and a longitudinal length of 4.5 cm. The chamber walls curve inwardly in one direction, with a central distance of 0.5 cm, and outwardly in a perpendicular direction, with a maximum central distance of 4.5 cm, to maintain a constant cross-sectional area. Two substrate surfaces were located on the top and bottom chamber walls at exactly the middle point of the reactor. The horizontal dimensions of the substrates were 1.5 cm by 0.7 cm. Due to the wall curving of the chamber, the two parallel surfaces of the substrates were separated by 0.5 cm. The walls of the reactor were quartz glass (fused silica) and the substrates are made of transparent sapphire. The background temperature selected for the simulations was 300K and for the substrate temperature was 773K. The flow rates chosen were 10 standard liter per minute for N_2, and 0.35 and 50 standard cubic centimeters per minute for TMI and NH_3, respectively. The computations were performed assuming terrestrial gravity. The numerical simulations were performed in two dimensions and because of the axial symmetry of the reactor, only half of it was modeled. The simulations were carried out under steady-state and time-dependent conditions.

Seven steady-state cases were studied. Case 1 and case 2 consisted of mechanism I with no adduct formation and with adduct formation but no adduct dissociation, respectively; cases 3 through 5 consisted of mechanism II with no adduct formation, with adduct formation and no adduct dissociation, and with adduct formation and adduct dissociation, respectively. Cases 6 and 7 consisted of mechanism III with no adduct formation and with adduct formation but no adduct dissociation. Three time-dependent simulations were performed, involving a pulsing process, in which the following sequence of gas mixture was introduced into the reactor chamber every 2/10 s: $N_2 + NH_3$; N_2; N_2 + TMI; N_2. The chemical pulsing cases studied consisted of mechanism II with no adduct formation (case 8), with adduct formation but no adduct dissociation (case 9), and with adduct formation and adduct dissociation (case 10).

InN film formation for cases 1, 3 and 6, was predominantly due to the deposition of InN generated in the gas phase. In terms of the overall InN film growth rate, the results for these three cases were essentially the same (see Figure 8). Formation of adduct (without allowing for dissociation) substantially reduced the available TMI and, consequently, the InN film growth rate.

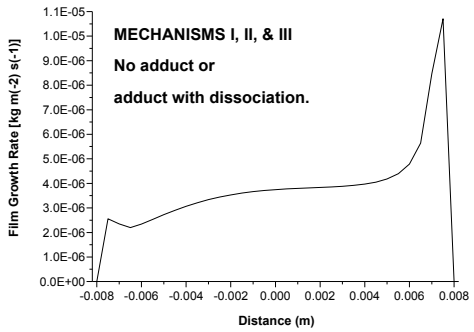

Figure 8. InN film growth rate at the substrate for mechanism I (case 1), mechanism II (case 3), and mechanism III (case 5), when no adduct formation was included.
(The coordinate system origin is at the center of the substrate.)

Figure 9 shows that inclusion of adduct formation (cases 2, 4 and 7) prevented film growth by several orders of magnitude, when compared to cases 1, 3 and 4, and that film growth increased with MMI (case 4) and TMI (case 7) adsorption. When the adduct was allowed to dissociate, the growth rate was comparable to the case with no adduct formation.

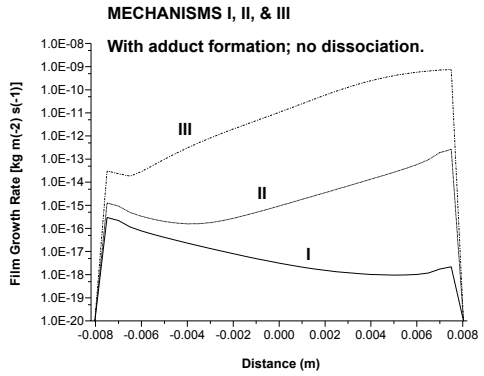

Figure 9. InN film growth rate at the substrate for mechanism I (case 2), mechanism II (case 4), and mechanism III (case 7), when adduct formation was included but no adduct dissociation was allowed.

Figure 10 shows that the mass fraction of adduct becomes considerably smaller (as compared to case 4) when the adduct was allowed to dissociate (case 5). In case 4, TMI was essentially tied up in the adduct. Thus, when the adduct was allowed to dissociate, it became a source of TMI for InN film growth. Figure 11 shows that vapor deposition was the main contributor to film growth under steady-state conditions.

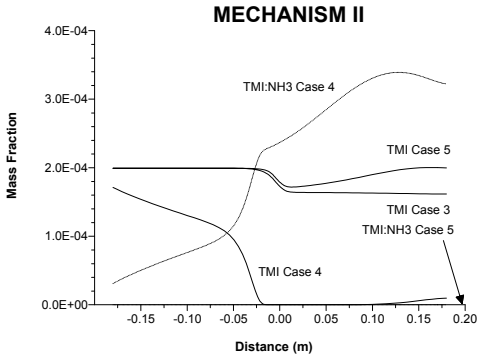

Figure 10. Mass fraction of TMI and TMI:NH_3 adduct for mechanism II, cases 3, 4 and 5.

Formation of the TMI:NH_3 adduct may be prevented by chemical pulsing, where TMI is separated from NH_3. Using mechanism II, three different cases were simulated (cases 8, 9, and 10)

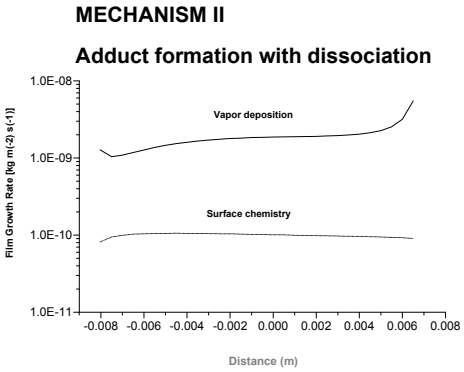

Figure 11. InN film growth rates from vapor deposition and from heterogeneous chemistry for mechanism II case 5.

which are the counterpart of the steady state cases 3, 4, and 5. Case 8 can be viewed as the ideal case in which no adduct formation was present. Case 9 represented the least favorable condition in which the TMI:NH_3 adduct acted as a permanent sink of the InN precursors. Case 10 was the one closest to reality, where the adduct was formed (therefore acting as a sink) but also it was allowed to dissociate, and consequently acting as a source of InN precursors. The results indicated that adduct formation with dissociation attained about 88% of the ideal value, while adduct formation with no dissociation attained only about 33% of the ideal value. When chemical pulsing was used, the heterogeneous reactions were the dominant mechanisms for InN film growth. Chemical pulsing enhanced surface chemistry; and the separation of TMI from NH_3 favored heterogeneous chemistry (more MMI became adsorbed and available for the arrival of NH) since the gas flow tended to keep TMI and NH_3 separate in the gas phase. Figure 12 compares the InN film growth rate from vapor deposition and from heterogeneous chemistry during two complete cycles. It can be seen that periodicity was achieved after the second cycle. Figure 12 also shows a short-lived InN peak that occured briefly after the regular occurrence of the InN film growth period. This short-lived film growth occured when an NH_3 pulse reached the substrate at a moment where the substrate was loaded with adsorbed MMI. At the moment of the arrival of the front of the NH_3 pulse, the second section of the substrate had an MMI concentration that was several orders of magnitude higher than the MMI concentrations present at the first half of the substrate. As the NH_3 reached the vicinity of the substrate, it very quickly photolyzed

into NH. As NH encountered the large MMI-adsorbed concentrations, it reacted to form InN film. The MMI-NH adsorbed complex depleted the MMI-adsorbed concentrations; this explains the short lifetime of the second InN peak.

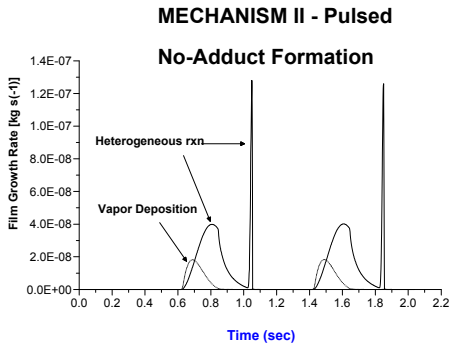

Figure 12. InN film growth rates from vapor deposition and from heterogeneous chemistry for pulsed mechanism II and no adduct formation (case 7)

Figure 13 shows the time history of the surface values at the middle of the substrate for two cycles of pulses. For each cycle, the first pulse of NH_3 was transported to the substrate and became decomposed into NH. Following the N_2 pulse, the TMI pulse was transported to the substrate where it was thermally decomposed by the substrate high temperature and MMI became adsorbed. Heterogeneous reactions took place where residual NH reacted with the adsorbed MMI to form InN. In a similar fashion, MMI in the gas phase reacted with NH to form gaseous InN. A portion of this InN was incorporated into the surface via vapor deposition. These simulations of cases 8, 9 and 10 indicate that: a) chemical pulsing significantly reduced the negative effect of adduct formation; b) surface chemistry was the dominant source of InN film growth; and c) adduct decomposition increased InN film growth by producing InN precursors.

4. Conclusions.

The gas-phase dissociation of trimethylindium (TMI) has been studied using three models: a strictly thermodynamic model, a strictly chemical kinetic model, and a chemical kinetic/fluid dynamic model based on an existing compact hard-shell reactor. The strictly thermodynamic model predicted dissociation of TMI at 300 K, in disagreement with experimental evidence. The strictly chemical kinetic model

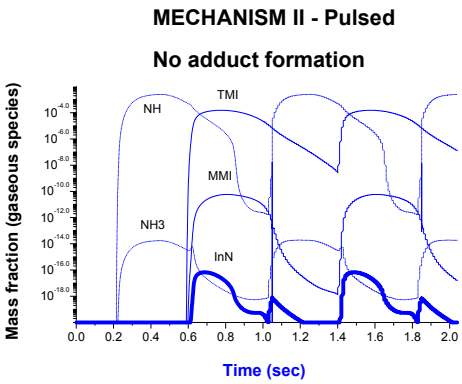

Figure 13. Mass fraction of several gaseous species for pulsed mechanism II and no adduct formation (case 8) immediately above the center of the substrate.

predicted no dissociation of TMI at 300 K, 4% dissociation at 850 K and 72% dissociation at 1000 K. The model predicted about twice as much monomethylindium (MMI) than atomic indium, at atmospheric pressure and at 20 atm, when the temperature was 1000 K. Finally, the chemical kinetic / fluid dynamic model, with a substrate temperature of 1000 K, indicated that the relative species concentrations were highly dependent on pressure. In all cases, dimethylindium (DMI) concentrations were negligible. At 1 atm, the model predicted 40% TMI and 58% MMI. A maximum of 93% MMI was predicted for 2.5 atm. For pressures above 12.5 atm, it was found that atomic indium (In) concentrations were greater than those of MMI. These predictions will be tested experimentally using the compact hard-shell reactor for high pressures of Georgia State University.

A chemical kinetic / fluid dynamic model was designed, based on a simplified system of chemical equations that would represent the reaction of TMI with ammonia (NH_3) and the deposition of InN. The simulations were conducted at atmospheric pressure, under standard gravity, using inlet gases at 300 K, and a substrate temperature of 773 K. The flow rates used were 10 standard liters per minute of nitrogen gas and, 0.35 and 50 standard cubic centimeters per minute for TMI and ammonia, respectively. Formation of TMI:NH_3 complex occurred in the gas phase, while the thermal decomposition of TMI either occurred in the gas phase or on TMI molecules adsorbed to the substrate. MMI and NH were the two reactive species selected for the formation of InN. InN could be formed either in the gas phase and subsequently adsorbed to the substrate, or by direct reaction of an adsorbed MMI with gaseous NH. The

incoming reactants (TMI and NH_3) were introduced into the reactor simultaneously or in pulses separated by N_2. The simulations indicated that if the adduct could dissociate, film growth was comparable to the case when no adduct formation was allowed. In addition, MMI and TMI adsorption enhanced film growth. Chemical pulsing enhanced surface chemistry, since the separation of TMI from NH_3 favored heterogeneous chemistry. In this case, more MMI became adsorbed and available for the arrival of NH at the substrate. The model provided concrete details regarding the periodicity of the deposition process, which will be tested experimentally using the reactor at Georgia State University.

Acknowledgments

The authors would like to acknowledge partial support of this work by NASA grant NAG8-1686 and NSF grant CHE-0213467.

References

[1] O. Ambacher; "Growth and applications of Group III-nitrides"; Journal of Physics D 31 (20), 2653-2710 (1998).

[2] S. C. Jain, M. Willander, J. Narayan, R. Van Overstraeten; "III-Nitrides: Growth, characterization, and properties"; Journal of Applied Phys. 87, 965-1006 (2000).

[3] S. J. Pearton, J. C. Zolper, R. J. Shul, F. Ren; "GaN: Processing, defects, and devices"; Journal of Applied Physics 86(1), 1-78 (1998).

[4] A. G. Bhuiyan, A. Hashimoto, A. Yamamoto; "Indium nitride (InN): A review on growth, characterization and properties"; Journal of Applied Physics 94(5), 2779-2808 (2003).

[5] J. Cai, F. A. Ponce; "Study of charge distribution across interfaces in GaN/InGaN/GaN single quantum wells using electron holography"; Journal of Applied Physics 91, 9856-9862 (2002).

[6] S. N. Mohammad, H. Morkoc; "Progress and prospects of group-III nitride semiconductors"; Progress in Quantum Electronics, 20, 361-525 (1996).

[7] T. L. Tansley, C. P. Foley; "Optical band gap of indium nitride"; Journal of Applied Physics 85(9), 3241-3244 (1986)

[8] V.Yu. Davydov, A.A. Klochikhin, R.P. Seisyan, V.V. Emtsev, S.V. Ivanov, F. Bechstedt, J. Furthmüller, H. Harima, A.V. Mudryi, J. Aderhold, O. Semchinova, J. Graul; "Absorption and Emission of Hexagonal InN. Evidence of Narrow Fundamental Band Gap"; Physica Status Solidi B, 229 (3), R1-R3 (2002)

[9] V.Yu. Davydov, A.A. Klochikhin, V.V. Emtsev, S.V. Ivanov, V.V. Vekshin, F. Bechstedt, J. Furthmüller, H. Harima, A.V. Mudryi, A. Hashimoto, A. Yamamoto, J. Aderhold, J. Graul, E.E. Haller; "Band Gap of InN and In-Rich InxGa1 - xN alloys ($0.36 < x < 1$)"; Physica Status Solidi B 230 (2), R4-R6 (2002)

[10] D. W. Jenkins, J. D. Dow; "Electronic structures and doping of InN, InxGa1-xN and InxAl1-xN"; Physics Review B 39(5), 3317- 3329 (1989).

[]11 V.Yu. Davydov, A.A. Klochikhin, V.V. Emtsev, D.A. Kurdyukov, S.V. Ivanov, V.A. Vekshin, F. Bechstedt, J. Furthmüller, J. Aderhold, J. Graul, A.V. Mudryi, H. Harima, A. Hashimoto, A. Yamamoto, E.E. Haller; "Band Gap of Hexagonal InN and InGaN Alloys"; Physica Status Solidi B 234 (3), 787-795 (2002).

[12] V.V. Mamutin, V.A. Vekshin, V.Yu. Davydov, V.V. Ratnikov, Yu.A. Kudriavtsev, B.Ya. Ber, V.V. Emtsev, S.V. Ivanov; "Mg-Doped Hexagonal InN/Al2O3 Films Grown by MBE"; Physica Status Solidi A 176 (1), 373-378 (1999).

[13] Lu, Hai; Schaff, William J.; Hwang, Jeonghyun; Eastman, Lester F.; "Preparation of InN and InN-based heterostructures by molecular beam epitaxy"; Proceedings 2001 MRS Spring Meeting; Materials Research Society Symposium 680E, E3.2 (2001).

[14] A. Yamamoto, T. Tanaka, K. Koide, A. Hashimoto; "Improved Electrical Properties for Metalorganic Vapour Phase Epitaxial InN Films"; Physica Status Solidi A 194 (2), 510-514 (2002).

[15] H. Lu, W. J. Schaff, L. F. Eastman, J. Wu, W. Walukiewicz, K. M. Yu, J. W. Auger III, E. E. Haller; "Electrical and optical properties of InN grown by MBE"; The 44th Electronic Materials Conference (June 26-28, 2002, Santa Barbara, CA), A 4. Values reported by Bhuiyan et al., reference 4.

[16] D. C. Look, D. C. Reynolds, J. W. Hemsky, J. R. Sizelove, R. L. Jones, R. J. Molnar; "Defect donor and acceptor in GaN"; Physical Review Letters 79 (12) 2273-2276 (1997).

[17] T. Yodo, H. Yona, H. Ando, D. Nosei; "Strong band luminescence from InN films grown on Si substrates by electron cyclotron resonance-assisted molecular beam epitaxy"; Applied Physics Letters 80 (6), 968-970 (2002)

[18] O. Ambacher, M. S. Brandt, R. Dimitrov, T. Metzger, M. Stutzmann, R. A. Fischer, A. Miehr, A. Bergmajer, G. Dollinger; “Thermal stability and desorption of Group III nitrides prepared by metal organic chemical vapor deposition”; Journal of Vacuum Science & Technology B 14 (6), 3532- 3542 (1996).

[19] G. B. Stringfellow; “A critical appraisal of growth mechanisms”; Journal of Crystal Growth 68 (1), 111-122 (1984); “Thermodynamic aspects of organometallic vapor phase epitaxy”; 62 (2), 225-229 (1983).

[20] H. Seki, A. Koukitu; “Thermodynamic analysis of metalorganic vapor phase epitaxy of III-V alloy semiconductors”; Journal of Crystal Growth 74 (1), 172-180 (1986); A. Koukitu, H. Seki; “Thermodynamic analysis of the MOVPE growth of quaternary III-V alloy semiconductors”; Journal of Crystal Growth 76 (2) 233-242 (1986).

[21] T. J. Mountziaris, K. F. Jensen; “A kinetic model for metalorganic chemical vapor deposition of gallium arsenide from trimethylgallium and arsine”; Materials Research Society Symposium Proceedings 131 (in “Chemical Perspectives of Microelectronic Materials”; edited by M. E. Gross, J. Jasinski, J. T. Yates), 117-22. (1989)

[22] R. Asai, D. S. Dandy; “Thermodynamic analysis of III–V semiconductor alloys grown by metalorganic vapor phase epitaxy”; Journal of Applied Physics 88 (7), 4407-4416 (2000).

[23] R. A. Talalaev, E. V. Yakovlev, S. Yu. Karpov, Yu. N. Makarov, O. Schoen, M. Heuken, G. Strauch, H. Juergensen; “Modeling of InGaN MOVPE in AIX 200 Reactor and AIX 2000 HT Planetary Reactor”; MRS Internet Journal Nitride Semiconductor Research 4, article 5 (1999).

[24] CHEMKIN Software: http://www.reactiondesign.com/ps_chemkin.html;

[25] R. W. Carr; “Computational chemistry in detailed chemical kinetics modeling of complex reactive systems”; University of Minnesota, Supercomputing Institute, Spring 2001 Research Bulletin, Vol. 17, No. 2.

[26] CFD-ACE; CFD Research Corporation, Huntsville, AL 35805.

[27] A. Krishnan, N. Zhou; “Analysis of chemical vapor deposition in industrial reactors”; 4th ASME/JSME Thermal Engineering Conference, Hawaii, March 1995.

[28] N. Zhou, A. Krishnam, A.J. Przekwas; “A computational model for chemical vapor deposition processes in industrial reactors”; 4th Intersociety Conference on Thermal Phenomena in Electronic Systems; 222-236, Washington D.C., May 1994

[29] B. H. Cardelino, C. E. Moore, C. A. Cardelino, D. O. Frazier, K. J. Bachmann; “Theoretical study of indium compounds of interest for organometallic chemical vapor deposition”; Journal of Physical Chemistry A 105 (5), 849-868 (2001)

[30] Chase, M. W.; “JANAF Thermochemical Tables”; American Chemical Society (Washington, DC) and American Institute of Physics (New York, NY) for the National Bureau of Standards; issued as Supplement #1 to Volume 14 of the Journal of Physical and Chemical Reference Data; 3rd edition, 1986.

[31] Gaussian03; M. J. Frisch, G. W. Trucks, H. B. Schlegel, G. E. Scuseria, M. A. Robb, J. R. Cheeseman, V. G. Zakrzewski, J. A. Montgomery, Jr., R. E. Stratmann, J. C. Burant, S. Dapprich, J. M. Millam, A. D. Daniels, K. N. Kudin, M. C. Strain, O. Farkas, J. Tomasi, V. Barone, M. Cossi, R. Cammi, B. Mennucci, C. Pomelli, C. Adamo, S. Clifford, J. Ochterski, G. A. Petersson, P. Y. Ayala, Q. Cui, K. Morokuma, P. Salvador, J. J. Dannenberg, D. K. Malick, A. D. Rabuck, K. Raghavachari, J. B. Foresman, J. Cioslowski, J. V. Ortiz, A. G. Baboul, B. B. Stefanov, G. Liu, A. Liashenko, P. Piskorz, I. Komaromi, R. Gomperts, R. L. Martin, D. J. Fox, T. Keith, M. A. Al-Laham, C. Y. Peng, A. Nanayakkara, M. Challacombe, P. M. W. Gill, B. Johnson, W. Chen, M. W. Wong, J. L. Andres, C. Gonzalez, M. Head-Gordon, E. S. Replogle, and J. A. Pople, Gaussian, Inc., PA, (2003).

[32] B. H. Cardelino, C. E. Moore, C. A. Cardelino, S. D. McCall, D. O. Frazier, K. J. Bachmann; "Semiclassical calculation of reaction rate constants for homolytical dissociation reactions of interest in OMCVD"; J. Physical Chemistry A 107, 3708-3718 (2003).

[33] C. A. Cardelino, C. E. Moore, B. H. Cardelino, N. Zhou, S. A. Lowry, A. Krishnan, D. O. Frazier, K. J. Bachmann; “Development of an advanced computational model for OMCVD of indium nitride”**;** Proceedings of SPIE-The International Society for Optical Engineering, 3625 (Physics and Simulation of Optoelectronic Devices VII), 447-458 (1999).